J. Am. Chem. Soc. **1996,** *118,* 5020−5030

Electrochemical Oxidation and Structural Changes of 5,6-Dihydrobenzo[*c*]cinnolines

Michael Dietrich,† Jürgen Heinze,*,† Claus Krieger,‡ and Franz A. Neugebauer*,‡

Contribution from the Institut für Physikalische Chemie, Universität Freiburg, Albertstrasse 21, D-79104 Freiburg, and Max-Planck-Institut für medizinische Forschung, Abteilung Organische Chemie, Jahnstrasse 29, D-69120 Heidelberg, Germany

Received August 10, 1995. Revised Manuscript Received February 13, 1996⊗

Abstract: The anodic oxidation of tetraphenylhydrazine (**1**) and various 5,6-dihydrobenzo[*c*]cinnoline derivatives (**2**−**10**) in liquid SO_2 and CH_2Cl_2 was studied by cyclic voltammetry at different temperatures. All compounds could be oxidized to their respective dications and in some cases to their trications. The unusual results indicate a high internal reorganization energy during the first oxidation step. X-ray structure determinations and other findings reveal that the electron transfer reactions are accompanied by structural changes of the molecular framework. The mechanism of oxidation will be dicussed in terms of different variants. Digital simulations and experimental data give strong evidence for an E_iE−DISP mechanism.

1. Introduction

The oxidation of hydrazines with a gauche or an antiperiplanar orientation of the adjacent lone-pair orbitals on the N atoms leads to radical cations with a nearly planar structural framework. This flattening in the oxidized state can be explained by a change in the hybridization of the N atoms from a sp^3 to a sp^2 state. The destabilizing repulsive interaction between the lone pairs in the neutral molecules is replaced by a stabilizing three-electron−two-orbital bonding interaction in the radical cations.[1]

The electrochemical behavior of cyclic aliphatic hydrazines was intensively investigated by Nelsen and Evans et al. by means of cyclic voltammetry.[2] They attributed their experimental findings to the existence of two different conformers with an axial, equatorial (ae) or an equatorial, equatorial (ee) arrangement of the substituents in the neutral state of the molecules, like 1,2-dimethylhexahydropyridazine (Figure 1), and proposed a triangular reaction scheme. During cyclic voltammetric experiments, both conformers are oxidized to the same radical cation, but the reduction of this cation (in the reverse scan) leads only to the ee conformer. The standard potentials for the oxidation of the ee and the ae conformers are almost the same, but there is a big difference in the heterogeneous rate constants of the two oxidation processes. The oxidation of the ae conformer takes place at a much slower rate than the corresponding electron transfer with the ee conformer. Nelsen and Evans explain this by a higher internal reorganization energy of the ae conformer during the oxidation process. According to this model, the conformational flattening of the molecular framework takes place simultaneously with the charge transfer and is an indirect measure of the internal reorganization energies that are connected with the conformational changes.

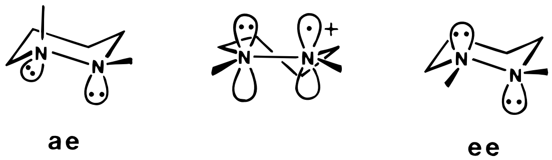

Figure 1. 1,2-Dimethylhexahydropyridazine: ee and ae conformations and the flattened structure of its radical cation.

A similar mechanism (E_iE−DISP) with simultaneous electron transfer and conformational flattening of the molecular framework is discussed for the reduction of cyclooctatetraene.[3−5]

In contrast to this, a quadratic reaction scheme is favored for the reduction of bianthrone derivatives. In this case, both equilibrium conformers are first reduced to their respective radical anions, followed by the transformation to the thermodynamically most stable anion conformer.[6−8]

With regard to the oxidation of aryl-substituted hydrazines, only the radical cations formed first have so far been described as persistent species.[9−18] To our knowledge, however, nothing is known about the particular conformational effects in the

---

† Universität Freiburg.

‡ Max-Planck-Institut.

⊗ Abstract published in *Advance ACS Abstracts,* May 1, 1996.

(1) (a) Nelsen, S. F.; Hintz, P. J. *J. Am. Chem. Soc.* **1972**, *94*, 7108−7113. (b) Nelsen, S. F.; Weisman, G. R.; Hintz, P. J.; Olp, D.; Fahey, M. R. *J. Am. Chem. Soc.* **1974**, *96*, 2916−2923. (c) Nelsen, S. F. Hydrazine, Hydrazine Cation Radical Electron Transfer Reactions. In *Molecular Structures and Energetics*; Liebman, J. F., Greenberg, A., Eds.; VCH Publishers, Inc.: Deerfield Beach, FL, 1986; Vol. 3, Chapter 1, p 1.

(2) (a) Nelsen, S. F.; Echegoyen, L.; Evans, D. H. *J. Am. Chem. Soc.* **1975**, *97*, 3530−3532. (b) Nelsen, S. F.; Echegoyen, L.; Clennan, E. L.; Evans, D. H.; Corrigan, D. A. *J. Am. Chem. Soc.* **1977**, *99*, 1130−1134. (c) Nelsen, S. F.; Clennan, E. L.; Evans, D. H. *J. Am. Chem. Soc.* **1978**, *100*, 4012−4019.

(3) Allendoerfer, R. D.; Rieger, P. H. *J. Am. Chem. Soc.* **1965**, *87*, 2336−2344.

(4) Huebert, B. J.; Smith, D. E. *J. Electroanal. Chem.* **1971**, *31*, 333−348.

(5) Smith, W. H.; Bard, A. J. *J. Electroanal. Chem.* **1977**, *76*, 19−26.

(6) Hammerich, O.; Parker, V. D. *Acta Chem. Scand., Ser. B* **1981,** *35*, 395−402.

(7) (a) Olsen, B. A.; Evans. D. H. *J. Am. Chem. Soc*. **1981**, *103*, 839−843. (b) Olsen, B. A.; Evans, D. H.; Agranat, I. *J. Electroanal. Chem.* **1982**, *136*, 139−148.

(8) (a) Matsue T.; Evans, D. H.; Agranat, I. *J. Electroanal. Chem.* **1984**, *163*, 137−143. (b) Matsue, T.; Evans, D. H. *J. Electroanal. Chem.* **1984**, *168*, 287−298.

(9) (a) Neugebauer, F. A.; Bock, M.; Kuhnhäuser, S.; Kurreck, H. *Chem. Ber.* **1986**, *119*, 980−990. (b) Neugebauer, F. A.; Kuhnhäuser, S. *Angew. Chem., Int. Ed. Engl.* **1985**, *24*, 596−597; *Angew. Chem.* **1985**, *97*, 589−590.

(10) (a) Cauquis, G.; Genies, M. *Tetrahedron Lett.* **1971**, 3959−3962. (b) Cauquis, G.; Delhomme, H.; Serve, D. *Tetrahedron Lett.* **1971**, 4649−4652. (c) Cauquis, G.; Genies, M.; Serve, D. *Tetrahedron Lett.* **1972**, 5009−5012. (d) Cauquis, G.; Chabaud, B.; Genies, M. *Bull. Soc. Chim. Fr.* **1973**, 3482−3486. (e) Cauquis, G.; Delhomme, H.; Serve, D. *Electrochim. Acta* **1975**, *20*, 1019−1026.

(11) Svanholm, U.; Parker, V. D. *J. Am. Chem. Soc.* **1972**, *94*, 5507−5508.

S0002-7863(95)02722-3 CCC: $12.00

Chart 1

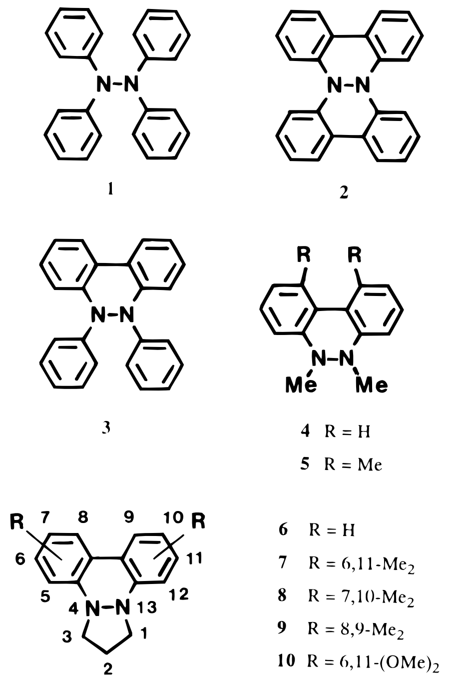

1

2

3

4 R = H

5 R = Me

6 R = H

7 R = 6,11-Me$_2$

8 R = 7,10-Me$_2$

9 R = 8,9-Me$_2$

10 R = 6,11-(OMe)$_2$

course of the oxidation of these hydrazines, which can be traced by electrochemical methods. Recently, we observed an unexpected "two-electron" transfer in the cyclic voltammogram of 5,6-dihydro-5,6-diphenylbenzo[*c*]cinnoline (**3**) and, furthermore, demonstrated the reversible formation of the mono-, di-, and trications of benzo[*c*]benzo[3,4]cinnolino[1,2-*a*]cinnoline (**2**) in liquid sulfur dioxide.[19] Encouraged by these findings, we comprehensively investigated the anodic oxidation of tetraphenylhydrazine (**1**) and various 5,6-dihydrobenzo[*c*]cinnoline derivatives (**2**−**10**) by cyclic voltammetry and digital simulation and elucidated a general electrochemical reaction mechanism for this class of compounds. Furthermore, not only the heterogeneous but also the homogeneous (disproportionation) rate constants for the oxidation of the hydrazines could be determined, and relationships between the thermodynamic and kinetic parameters of the redox processes and the structural characteristics of the molecules were established.

2. Experimental Section

Materials. The compounds tetraphenylhydrazine (**1**),[20] benzo[*c*]benzo[3,4]cinnolino[1,2-*a*]cinnoline (**2**),[9] 5,6-dihydro-5,6-diphenylbenzo[*c*]cinnoline (**3**),[9] 5,6-dihydro-5,6-dimethylbenzo[*c*]cinnoline (**4**),[9a] 5,6-dihydro-1,5,6,10-tetramethylbenzo[*c*]cinnoline (**5**),[18b] 2,3-dihydro-1*H*-benzo[*c*]pyrazolo[1,2-*a*]cinnoline (**6**),[21] 2,3-dihydro-6,11-dimethyl-1*H*-benzo[*c*]pyrazolo[1,2-*a*]cinnoline (**7**),[22] 2,3-dihydro-7,10-dimethyl-1*H*-benzo[*c*]pyrazolo[1,2-*a*]cinnoline (**8**),[22] 2,3-dihydro-8,9-dimethyl-1*H*-benzo[*c*]pyrazolo[1,2-*a*]cinnoline (**9**),[22] and 2,3-dihydro-6,11-dimethoxy-1*H*-benzo[*c*]pyrazolo[1,2-*a*]cinnoline (**10**)[22] were available in our laboratory or were prepared as described in the literature.

Table 1. Crystallographic Data and Refinement Parameters of **3** and **10**

	3	**10**
formula	$C_{24}H_{18}N_2$	$C_{17}H_{18}N_2O_2$
fw	334.42	282.35
crystal system	orthorhombic	monoclinic
space group	*Pbca*	$P2_1/n$
a, Å	12.667(3)	12.919(2)
b, Å	17.872(5)	5.519(1)
c, Å	15.642(3)	20.112(4)
b, deg		97.48(2)
V, Å^3	3541(3)	1422(1)
Z	8	4
F(000)	1408	600
D_{calcd}, g cm^{-3}	1.254	1.319
μ, cm^{-1}	0.687	0.817
no. of measd reflcns ($\sin\theta/\lambda \le 0.67$ Å^{-1})	4055	3269
no. of obsd reflcns [$I \ge 2\sigma(I)$]	1640	2211
refinement R/R_w[a]	0.055/0.033	0.082/0.067
max $\Delta\rho$, e Å^{-3}	0.16(4)	0.78(9)
crystal size, mm^3	0.1 × 0.2 × 0.2	0.2 × 0.3 × 0.4

[a] $R = \sum(|F_o| - |F_c|)/\sum|F_o|$, $R_w = \{[\sum w(|F_o| - |F_c|)^2]/[\sum w|F_o|^2]\}^{1/2}$.

NMR Results. ^{1}H (500 MHz) and ^{13}C NMR (126 MHz) data (CD_3CN, temperature range +72 to −38 °C) of **2**−**6** and of **9** are given in the supporting information.

X-ray Structure Determinations of Compounds 3 and 10. Single crystals of the colorless **3** and the yellow **10** were grown from methanol and ethyl acetate, respectively. Diffraction data were collected at 22 °C on an Enraf-Nonius CAD-4 circle diffractometer, using graphite-monochromated Mo Kα radiation (λ = 0.710 69 Å, $\omega-2\theta$ scanning technique). Lattice parameters were determined from least-squares fit using 30 reflections (θ range: 10−14°). The structures were solved by direct methods (MULTAN) and were refined by full-matrix least-squares minimizing $\sum w(\Delta F)^2$ with the weighting scheme $w = [\sigma(F)^2 + (0.03F_0)^2]^{-1}$. Hydrogen atoms were refined with isotropic and all other atoms with anisotropic temperature factors.[23] Atomic scattering factors and anomalous-dispersion corrections were taken from *International Tables for X-Ray Crystallography*.[24] The crystallographic data and the parameters of structure refinement are given in Table 1.[25]

Purification Procedures. Commercially available sulfur dioxide (SO_2, Messer−Griesheim) was condensed at −70 °C under nitrogen atmosphere in a glass vessel equipped with basic alumina (ICN, Super B1) and a magnetic stirrer. The vessel was then partly evacuated, and the solvent was refluxed for one-half hour in the temperature range between −40 and −10 °C, depending on the quality of the vacuum. After this procedure, SO_2 was condensed under vacuum conditions in a thoroughly dried flask and stored there prior to use at −70 °C.

Technical grade dichloromethane was stirred for several days with concentrated sulfuric acid. The organic phase was washed with water until all of the acid had been removed, followed by stirring with a 1 M aqueous sodium carbonate solution, and subsequently washed again with water. Then the solvent was successively dried over calcium chloride, potassium carbonate, and calcium hydride and finally distilled

---

(12) Forrester, A. R.; Hay, J. M.; Thomson, R. H. *Organic Chemistry of Stable Free Radicals*; Academic Press: London, 1968; p 123.

(13) Das, M. R.; Patankar, A. V.; Venkataraman, B. *Proc. Indian Acad. Sci.* **1961**, *A53*, 273−295.

(14) Abakumov, G. A.; Pomerantseva, L. L. *Zh. Obshch. Khim.* **1966**, *36*, 1921−1924; *J. Gen. Chem. USSR* **1966**, *36*, 1913−1915.

(15) Cheng, J.-D.; Shine, H. J. *J. Org. Chem.* **1975**, *40*, 703−710.

(16) Pankratov, A. N.; Morozov, V. L.; Mushtakova, S. P.; Il'yasov, A. V. *Izv. Akad. Nauk SSSR, Ser. Khim.* **1984**, 1483−1487; *Bull. Acad. Sci. USSR, Div. Chem. Sci.* **1984**, *33*, 1363.

(17) Berti, C.; Greci, L.; Andruzzi, R.; Trazza, A. *J. Org. Chem.* **1985**, *50*, 368−373.

(18) (a) Neugebauer, F. A.; Bamberger, S. *Chem. Ber.* **1972**, *105*, 2058−2067. (b) Neugebauer, F. A.; Weger, H. *J. Phys. Chem.* **1978**, *82*, 1152−1157.

(19) (a) Dietrich, M.; Heinze, J.; Fischer, H.; Neugebauer, F. A. *Angew. Chem., Int. Ed. Engl.* **1986**, *25*, 1021−1023; *Angew. Chem.* **1986**, *98*, 999−1000. (b) Dietrich, M.; Heinze, J. *J. Am. Chem. Soc.* **1990**, *112*, 5142−5145.

(20) Wieland H.; Gambarjan, S. *Ber. Dtsch. Chem. Ges.* **1906**, *39*, 1499−1506.

(21) Farnum, D. G.; Alaimo, R. J.; Dunston, J. M. *J. Org. Chem.* **1969**, *32*, 1130−1134.

(22) Neugebauer, F. A.; Fischer, H. *J. Chem. Soc., Perkin Trans. 2* **1989**, 1349−1353.

(23) B. A. Frentz and Associates Inc., Structure Determination Package, 4th revised edition, College Station, TX, and Enraf-Nonius, Delft, The Netherlands, 1982.

(24) *International Tables for X-Ray Crystallography*; Kynoch: Birmingham, England, 1974; Vol. IV.

(25) Atomic coordinates, bond lengths and angles, torsional angles, and thermal parameters have also been deposited at the Cambridge Crystallographic Data Center, England.

Table 2. Bond Distances, Bond Angles, and Torsional Angles of the Hydrazine Segment in **1**−**3** and **10**

	1[a]	**2**[b]	**3**	**10**
N−N, Å	1.390	1.437(2)	1.428(4)	1.369(3)
N−C(ar), Å	1.420 (av)	1.436(2) [C(A1)−N] 1.414(3) [C(B1)−N] 1.424(3) [C(A1′)−N′] 1.419(3) [C(B1′)−N′]	1.410(5) [N(5)−C(4a)] 1.416(5) [N(5)−C(A1)] 1.437(5) [N(6)−C(6a)] 1.437(5) [N(6)−C(B1)]	1.401(3) [N(4)−C(4a)] 1.400(4) [N(13)−C(12a)]
N−C(CH$_2$), Å				1.457(3) [N(4)−C(3)] 1.446(3) [N(13)−C(1)]
∠CNN, deg	116.8 (av)	109.4 [C(A1)NN′] 113.8 [C(B1)NN′] 110.1 [C(A1′)N′N] 113.3 [C(B1′)N′N]	114.5(3) [C(4a)N(5)N(6)] 115.0(3) [C(A1)N(5)N(6)] 111.0(3) [C(6a)N(6)N(5)] 111.6(3) [C(B1)N(6)N(5)]	106.7(2) [C(3)N(4)N(13)] 116.8(2) [C(4a)N(4)N(13)] 108.2(2) [C(1)N(13)N(4)] 116.5(2) [C(12a)N(13)N(4)]
∠CNC, deg	126.3 (av)	121.6 [C(A1)NC(B1)] 120.4 [C(A1′)N′C(B1′)]	124.0(3) [C(4a)N(5)C(A1)] 118.4(3) [C(6a)N(6)C(B1)]	118.8(2) [C(3)N(4)C(4a)] 121.0(2) [C(1)N(13)C(12a)]
α (av), deg	120.0	114.9 [N] 114.6 [N′]	117.8 [N(5)] 113.7 [N(6)]	114.1 [N(4)] 115.2 [N(13)]
∠CNNC, deg		−60.7 [C(A1)NN′C(B1′)] −59.1 [C(B1)NN′C(A1′)] 161.3 [C(A1)NN′C(A1′)] 79.0 [C(B1)NN′C(B1′)]	−98.5(3) [C(A1)N(5)N(6)C(6a)] −80.1(3) [C(4a)N(5)N(6)C(B1)]	37.3(2) [C(3)N(4)N(13)C(1)] −46.6(3) [C(4a)N(4)N(13)C(12a)] 177.7(1) [C(3)N(4)N(13)C(12a)] 173.0(2) [C(4a)N(4)N(13)C(1)]
θ,[c] deg	74.4	59.9	89.3	175.4

[a] Lit.[29a]; structure of β-molecule at 20 °C; data of α-molecules show no significant deviations. [b] Lit.[30] [c] Lone pair−lone pair twist angle assuming that the lone pair orbital axes bisect the CNC angles in a Newman projection down the N−N bond.[31]

Table 3. Selected Torsional Angles (deg) of **3** and **10** with esd's in Parentheses

3		**10**	
C(4)−C(4a)−N(5)−N(6)	143.5(4)	C(2)−C(1)−N(13)−N(4)	−26.0(2)
C(4)−C(4a)−N(5)−C(A1)	−66.5(4)	C(2)−C(1)−N(13)−C(12a)	−164.2(3)
C(10b)−C(4a)−N(5)−N(6)	−34.1(4)	C(2)−C(3)−N(4)−N(13)	−32.1(2)
C(10b)−C(4a)−N(5)−C(A1)	116.0(4)	C(2)−C(3)−N(4)−C(4a)	−166.6(3)
C(B1)−N(6)−C(6a)−C(7)	−86.3(3)	C(3)−N(4)−C(4a)−C(5)	−21.6(3)
C(B1)−N(6)−C(6a)−C(10a)	93.5(3)	C(3)−N(4)−C(4a)−C(8a)	164.8(2)
N(5)−N(6)−C(6a)−C(7)	142.7(3)	N(13)−N(4)−C(4a)−C(5)	−151.8(2)
N(5)−N(6)−C(6a)−C(10a)	−37.5(3)	N(13)−N(4)−C(4a)−C(8a)	34.6(3)
C(4a)−N(5)−C(A1)−C(A2)	−0.7(5)	C(8b)−C(12a)−N(13)−C(1)	164.7(2)
N(6)−N(5)−C(A1)−C(A6)	−32.7(4)	C(8b)−C(12a)−N(13)−N(4)	29.6(3)
N(5)−N(6)−C(B1)−C(B6)	−37.5(4)	C(12)−C(12a)−N(13)−C(1)	−20.0(3)
C(6a)−N(6)−C(B1)−C(B2)	12.7(5)	C(12)−C(12a)−N(13)−N(4)	−155.1(2)

under nitrogen atmosphere. The purified dichloromethane was stored in a thoroughly dried flask at 0 °C in the dark. The anodic potential limit with tetrabutylammonium hexafluorophosphate (TBAPF$_6$) as supporting electrolyte lies at +2.8 (vs Ag/AgCl).

Electrochemical Measurements. All electrochemical experiments were carried out in specially constructed cells containing an internal drying column with highly activated alumina.[26,27] The working electrode was a Pt disk sealed in soft glass (1.00 mm diameter). A Pt wire, wrapped around the glass of the working electrode, was used as the counterelectrode. The reference electrode was an Ag wire on which AgCl had been deposited electrolytically, immersed in the electrolyte solution.

Potentials were calibrated with ferrocene (+ 0.352 V vs Ag/AgCl). The measurements were performed with an AMEL Model 553 potentiostat and a PAR 175 programmer. Data were recorded with a Philips Model PM 8131 X−Y recorder. For the higher scan rates a Model TRC 4070 Krenz transient recorder was used.

Digital Simulations. Digital simulations were carried out using the implicit Crank−Nicolson technique. All boundary conditions were formulated implicitly.[28]

3. Results and Discussion

3.1. Crystal Structures of 1, 2, 3, and 10 and Conformations of 1−10 in Solution. Bond distances, bond angles, and torsional angles of the hydrazine segment in **1**, **2**, **3**, and **10** appear in Table 2, and further selected torsional angles of **3** and **10** are given in Table 3.

The crystal structure of tetraphenylhydrazine (**1**) has already been reported.[29] Owing to considerable delocalization of the nitrogen lone pairs of electrons into the adjacent phenyl substituents, the tertiary nitrogens are approximately planar [α (av) = 120°] and the N−N bond becomes remarkably short (1.39 Å). Lone-pair−lone pair repulsion is minimized as indicated by the θ torsion angle of the lone-pair orbital axes about the N−N bond, (∠nNN′n′) ≈ 75°. Substantial steric interaction of the adjacent phenyl substituents, on the other hand, leads to the observed enlargement of the C−N−C angle (126°) and to the phenyl torsion angles ranging from 10° to 40°.[29]

A similar orthogonal arrangement of the diphenylamino moieties is expected for **1** in solution, in order to comply with the low lone pair−lone pair repulsion and the steric requirements of the large phenyl substituents. There is no direct evidence of a restricted rotation in **1**, but ^{1}H-NMR studies of a derivative of **1**, i.e. tetrakis(3,5-di-*tert*-butylphenyl)hydrazine, showed a restricted rotation about the N−C bonds with a barrier of 9.2 kcal mol^{-1}.[18a] On oxidation to the corresponding radical cation $\mathbf{1}^{\bullet+}$, the molecular structure of **1** is completely changed to yield an approximately planar hydrazinium moiety with restricted rotations not only about the N−N bond but also about the N−C bonds within the ESR time scale.[9a,18a]

The X-ray crystal structure of **2** has been published elsewhere.[30] Surprisingly, **2** crystallizes as separate enantiomers in the chiral space group $P2_1$. The crystal structure reveals twist

---

(26) Kiesele, H. *Anal. Chem.* **1981**, *53*, 1952−1954.

(27) Hinkelmann, K.; Heinze, J.; Schacht, H.-T.; Field, J. S.; Vahrenkamp, H. *J. Am. Chem. Soc.* **1989**, *111*, 5078−5091.

(28) Störzbach, M.; Heinze, J. *J. Electroanal. Chem.* **1993**, *346*, 1.

(29) (a) Hoekstra, A.; Vos, A.; Braun, P. B.; Hornstra, J. *Acta Crystallogr., Sect. B* **1975**, *31*, 1708−1715. (b) Hoekstra, A.; Vos, A. *Acta Crystallogr., Sect. B* **1975**, *31*, 1722−1729.

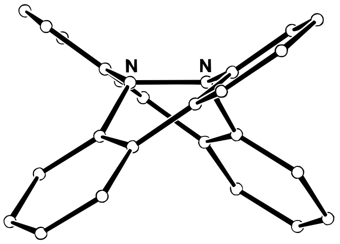

Figure 2. Molecular structure of **2** in the crystal.

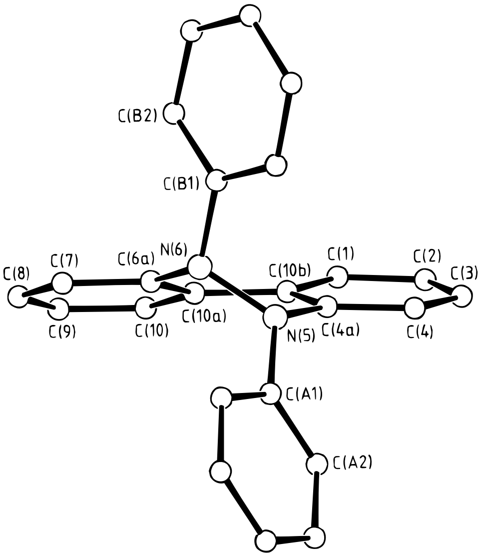

Figure 3. Molecular structure of **3** in the crystal with the atom-numbering scheme.

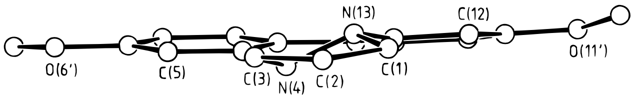

Figure 4. Molecular structure of **10** in the crystal in a side view along the molecular plane.

conformations for the 1,2-dihydropyridazine rings. Both nitrogens, showing slightly different geometries, are substantially nonplanar, α (av) ≈ 115°. The torsion angle θ about the N−N bond of about 60° corresponds to a favorably low lone pair−lone pair interaction. Racemization of **2** can occur by N−N axis rotation requiring double 1,2-dihydropyrazine ring reversal coupled with double biphenyl rotation and has the very high racemization barrier of 27.1 kcal mol^{-1} (pre-exponential factor $A = 6.52 \times 10^{14}$). The high racemization barrier is apparently related to strong steric interactions between the hydrogens in 1,17- and 8,10-positions (these are the 3,3′-hydrogens in the eclipsed 2,2′-biphenylene moieties, Figure 2), in addition to the lone pair−lone pair interaction in the transition state.[30] In the temperature range +70 to −38 °C, the ^{1}H and ^{13}C NMR data of **2** show no notable temperature dependence.

The crystallographic data of **3** are listed in Table 1, and the atom-numbering scheme of **3** is shown in Figure 3. Selected bond distances, bond angles, and torsional angles of this compound are given in the Tables 2 and 3. Due to the correlative substitution pattern at the hydrazine moiety in **3**, one might have expected a C_2 axis bisecting the N(5)−N(6) and C(10b)−C(10a) bonds. The geometry about both nitrogens, however, is found to be different. Derived from α (av) = 117.8°, N(5) appears to be nearly planar. The "p-rich" hybridization at this nitrogen is also pointed out by the relatively short bonds to C(4a) and C(A1). N(6), on the other hand, is substantially less flat, α (av) = 113.7°. The bonds to the adjacent C(6a) and C(B1) are a little longer (≈2%) than those of N(5), but still indicate some interaction of the electron lone pair with the coupled π-systems. The torsional angle θ between the lone-pair orbital axes of about 89° fits with the expected geometry for minimizing lone pair−lone pair repulsion. The central 1,2-dihydropyridazine ring exists in a twist conformation, where both phenyl substituents occupy pseudoaxial (a′) positions (Figure 3). This is clearly the sterically least hindered arrangement.

The steric situation of **3** suggests that the a′a′ conformer is also the predominant conformer in solution. ^{1}H and ^{13}C NMR data of **3** show no significant temperature dependence in the range +72 to −38 °C. This agrees with the presence of only the a′a′ conformer or with a′a′ $\rightleftharpoons$ a′e′ (nitrogen inversion) and a′a′ $\rightleftharpoons$ e′e′ (ring inversion) equilibria, which, for steric reasons, are shifted predominantly to the a′a′ side.

Compound **4** is sterically less restricted. Unfortunately its crystal structure is not known. For dissolved **4,** one expects a rapidly equilibrating a′e′ $\rightleftharpoons$ a′a′ $\rightleftharpoons$ e′a mixture by nitrogen inversion and, furthermore, the e′e′ conformer being accessible by ring inversion a′a′ $\rightleftharpoons$ e′e′. ^{1}H and ^{13}C NMR spectra of **4** in the temperature range +72 to −38 °C remain almost unchanged. Additional methyl substitution in the 2,9-positions, compound **5**, sterically impedes the ring inversion. Again the ^{1}H and ^{13}C NMR data in the range +72 to −38 °C show no significant changes.

Owing to the short trimethylene bridge in the 2,3-dihydro-1*H*-benzo[*c*]pyrazolo-[1,2-*a*]cinnoline series (**6**−**10**), a′a′ conformers are no longer possible. Of these compounds, only **10** provided crystals suitable for X-ray analysis. The crystallographic data and selected bond distances, bond angles, and torsional angles of **10** are given in the Tables 1−3. Its biphenyl-2,2′-diyl component is flatter than in **2** and **3**, thus giving the central 1,2-dihydropyridazine ring a half-twist conformation with substantially nonplanar nitrogens and an α (av) of 114.1° and 115.2°, respectively. The trimethylene bridge is attached to the nitrogens in e′ positions (Figure 4). Consequently, the torsional angle θ between both lone-pair orbital axes increases to 175°, leading to an unfavorably large lone pair−lone pair interaction, which effects the significant bending of the nitrogens from planarity. This adverse interaction seems to be caused in part by an increased lone pair−π-system interaction, indicated by relatively shorter N(4)−C(4a) and N(13)−C(12a) bond distances (1.40 Å). This view seems to be supported by the remarkably short N(4)−N(13) bond length of 1.369 Å. However, due to large thermal vibration of the nitrogens the N−N and N−C bond distances appear to be shorter than they are. The pronounced anisotropy of these vibrations leads to a maximal rms amplitude of 0.3 Å in the direction of the lone pairs, and the final R value of 0.082 reflects mainly the high residual electron density about the two nitrogens.

The crystal structure of **10** suggests that the e′e′ conformer may be the predominant one in solution. We cannot exclude, however, a rapidly equilibrating e′e′ $\rightleftharpoons$ a′e′ mixture. NMR studies of **6** and **9** in the range +72 to −38 °C showed no significant temperature dependence of the ^{1}H and ^{13}C signals.

3.2. Cyclic Voltammetry. (a) Tetraphenylhydrazine (1). The cyclic voltammetric investigation of **1** was carried out in liquid sulfur dioxide at temperatures between −20 and −40 °C. The compound dissolves in SO_2 with a deep yellow color.

At a temperature of −20 °C we succeeded in oxidizing **1** to

---

(30) Fischer, H.; Krieger, C.; Neugebauer, F. A. *Angew. Chem., Int. Ed. Engl.* **1986**, *25*, 374−375; *Angew. Chem.* **1986**, *98*, 341−342.

(31) (a) Nelsen, S. F.; Wang, Y.; Powell, D. R.; Hayashi R. K. *J. Am. Chem. Soc.* **1993**, *115*, 5246−5253. (b) Agmon, I.; Kaftory, M.; Nelsen, S. F.; Blackstock, S. C. *J. Am. Chem. Soc.* **1986**, *108*, 4477−4484.

the dication in two reversible oxidation steps ($E_1^0 = 0.795$ V, $E_2^0 = 1.645$ V). The electrochemically generated dication turned out to be stable within the time scale of the voltammetric experiment. At −40 °C, the standard potential of the dication formation shows a shift to $E = 1.620$ V.

The large potential interval between E_1^0 and E_2^0 suggests that the positive charges of the mono- and dication levels are localized mainly on the nitrogen atoms and that the second electron transfer is probably accompanied by a further internal molecular reorganization, i.e. an increased flattening of the central N−N framework. This is in accordance with the crystal structure of **1**[29] and the ESR-ENDOR results of the radical cation $\mathbf{1}^{\bullet+}$.[9a,18a] Derived from the ESR data, in $\mathbf{1}^{\bullet+}$, the *N*-phenyl rings are distorted about the N−C(ar) bond by ≈ 30°, and the N atoms each have a spin density of ca. 0.25.

(b) Benzo[*c*]benzo[3,4]cinnolino[1,2-a]cinnoline (2). Compound **2** was investigated in liquid sulfur dioxide in the temperature range of −20 and −70 °C and in dichloromethane at different temperatures between −10 and −80 °C.

Like **1**, the solution of **2** in liquid SO_2 showed a deep yellow color, while the dichloromethane solution was colorless.

At −50 °C in SO_2, we succeeded in generating the trication of **2** with a lifetime of 0.3 s. Under these conditions, the standard potentials for the mono-, di-, and trication formation are $E_1^0 = 0.560$ V, $E_2^0 = 1.165$ V, and $E_3^0 = 2.745$ V.

The standard potentials of the second and third oxidation steps are temperature dependent and show a shift of +1 mV °C^{-1}.

During the cyclic voltammetric experiments in dichloromethane, the reversible oxidation to the dication was observed at all mentioned temperatures. The standard potentials for the formation of the mono- and the dication at −40 °C are $E_1^0 = 0.485$ V and $E_2^0 = 1.180$ V.

The second standard potential shows a temperature-dependent shift of 0.5 mV °C^{-1}.

The first electron transfer during the oxidation of **2** occurs at a potential 240 mV lower than that of the corresponding oxidation of **1**. This shows that the formation of the radical cation $\mathbf{2}^{\bullet+}$ is thermodynamically easier than of $\mathbf{1}^{\bullet+}$ due to the better conjugation in the more planarized system and the stronger N-lone-pair repulsion of the neutral species. The completely bridged framework facilitates apparently also the second electron transfer, thus leading to a smaller interval between E_1^0 and E_2^0.

The solvent dependence of the first oxidation potential as well as the temperature dependence of the second and subsequent oxidation potentials were observed for all investigated hydrazines and will be discussed at the end of this section.

Neither **1** nor **2** exhibited any unusual behavior during the regular electrochemical investigations.

(c) 5,6 Dihydro-5,6-diphenylbenzo[*c*]cinnoline (3). Like the above-mentioned compounds, **3** also dissolves in liquid sulfur dioxide with a yellow color.

Its cyclic voltammogram at −50 °C and a sweep rate of 100 mV s^{-1} in the potential range between 0.0 and 1.48 V shows a high anodic wave at $E_{pa}^1 = 1.08$ V during the forward sweep, followed by two reduction waves at $E_{pc}^1 = 0.18$ V and $E_{pc}^2 = 0.81$ V in the reverse sweep (Figure 5a). Moreover, there is a trace crossing effect visible in the potential range between 0.88 and 0.94 V. If the scan is reversed before E_{pc}^1 is reached, a new oxidation wave at $E_{pa}^2 = 0.87$ V appears during the second and subsequent scans, while at the same time the oxidation wave at E_{pa}^1 loses intensity from cycle to cycle (Figure 5b). The oxidation wave at E_{pa}^2 and the reduction wave at E_{pc}^2 belong to the same redox pair with a standard potential of $E_2^0 = 0.840$ V.

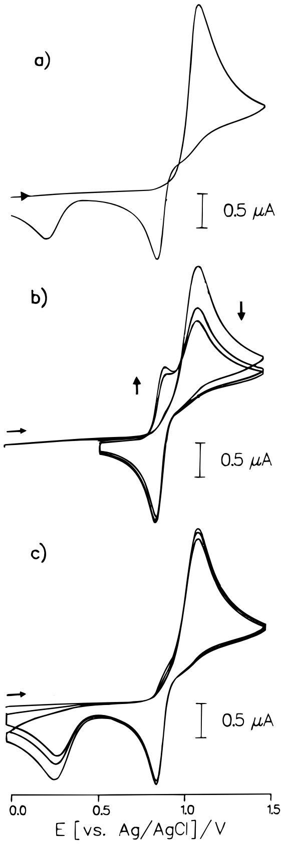

Figure 5. Cyclic voltammograms for the oxidation of **3** in liquid SO_2/0.1 M TBAPF$_6$, $T = -50$ °C, $v = 100$ mV s^{-1}, $c = 8 \times 10^{-4}$ M: (a) one-cycle voltammogram; (b) multisweep voltammogram between 0.6 and 1.45 V; (c) multisweep voltammogram between −0.05 and 1.45 V.

During multisweep experiments between −0.07 and +1.53 V no oxidation peak appeared that could be associated with the reduction peak at E_{pc}^1 (Figure 5c). There is even no change at −70 °and sweep rates up to 20 V s^{-1}.

A decrease in temperature or an increase in the scan rate leads to strong potential shifts of the oxidation peak at E_{pa}^1 in anodic direction and the reduction peak at E_{pc}^1 in cathodic direction, while the values of E_{pa}^2 and E_{pc}^2 change only slightly. The same is true of the cyclic voltammograms in dichloromethane. Figure 6 shows the cyclic voltammograms of **3** in CH_2Cl_2 at four different temperatures.

By changing the substrate concentration from 1×10^{-3} M to 4×10^{-3} M a current-shoulder at 0.900 V appears on the rising portion of the oxidation peak at E_{pa}^1 (Figure 7a).

Multisweep experiments at −80 °C in the potential range between 0.565 and 1.470 V show the same features as the corresponding voltammograms in liquid sulfur dioxide. During the second and the following cycles an additional oxidation wave at $E_{pa}^2 = 0.935$ V appears, which grows from cycle to cycle, while at the same time the oxidation wave at E_{pa}^1 loses intensity (Figure 8a). This new oxidation wave and the reduction wave at $E_{pc}^2 = 0.800$ V belong to the same redox pair with a standard potential of $E_2^0 = 0.870$ V.

At −30 °C, the oxidation peak at E_{pa}^2 decreases very rapidly from cycle to cycle and disappears completely at the end of the third cycle (Figure 8c).

A change of working electrode leads to different shapes of the cyclic voltammograms. Figure 7b shows a voltammogram of **3** in CH_2Cl_2 at a scan rate of 100 mV s^{-1} and a temperature of 20 °C in the potential range between 0.0 and 1.2 V using a

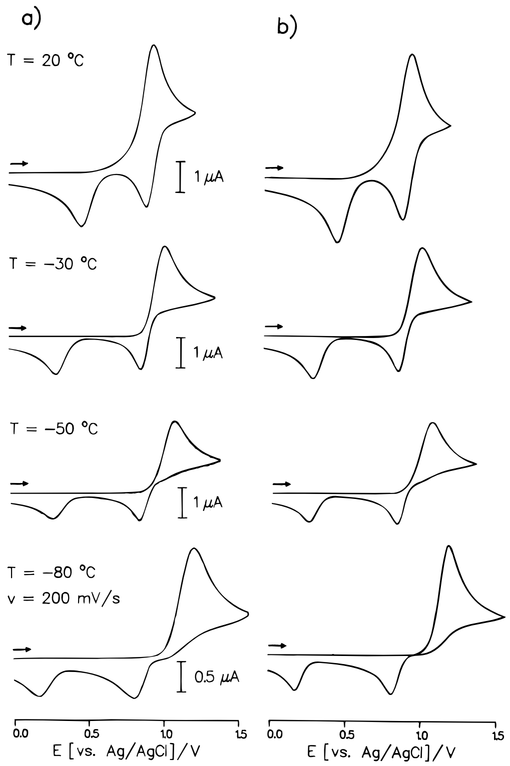

Figure 6. Experimental (a) and simulated (b) cyclic voltammograms of **3** in CH_2Cl_2 at four different temperatures, $v = 100$ mV s^{-1}, $c = 1.1 \times 10^{-3}$ M; specific simulation data in Table 4.

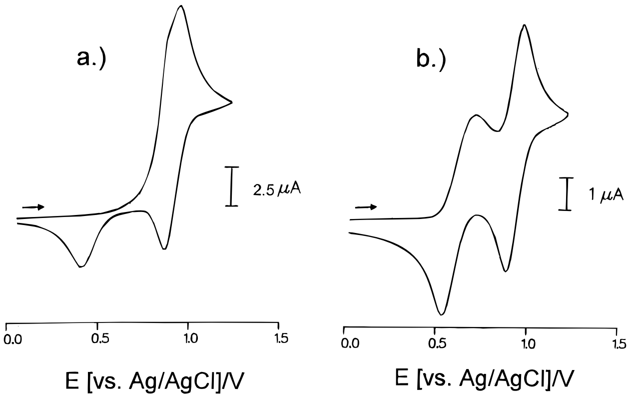

Figure 7. Experimental cyclic voltammograms of **3** in CH_2Cl_2/0.1 M TBAPF$_6$: (a) $c = 4 \times 10^{-3}$ M, $T = 20$ °C, $v = 100$ mV s^{-1}; (b) using a freshly annealed Pt wire electrode, $c = 1 \times 10^{-3}$ M, $T = 20$ °C, $v = 100$ mV s^{-1}. Simulations are given in the supporting information, specific simulation data in Table 4.

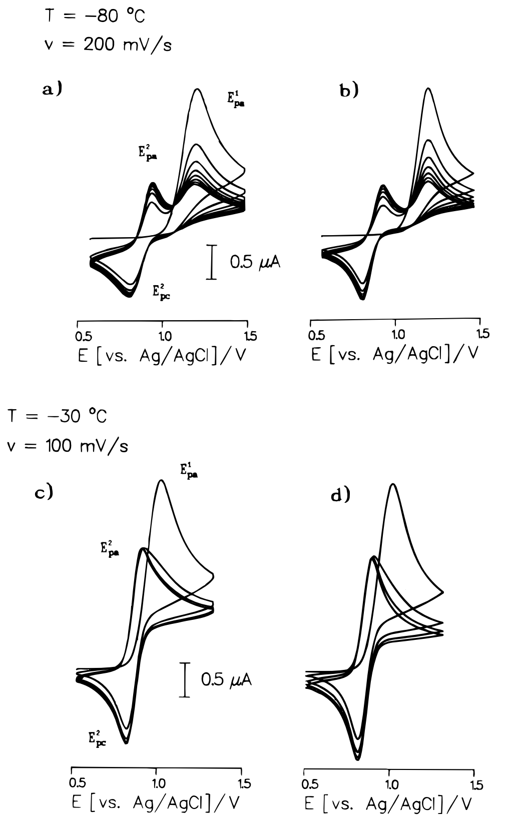

Figure 8. Multisweep voltammograms for the oxidation of **3** in CH_2Cl_2/0.1 M TBAPF$_6$, c = 1.1×10^{-3} M: (a) experiment, $T = -80$ °C, $v = 200$ mV s^{-1}; (b) simulation of a, parameters in Table 4; (c) experiment, $T = -30$ °C, $v = 100$ mV s^{-1}; (d) simulation of c, parameters in Table 4.

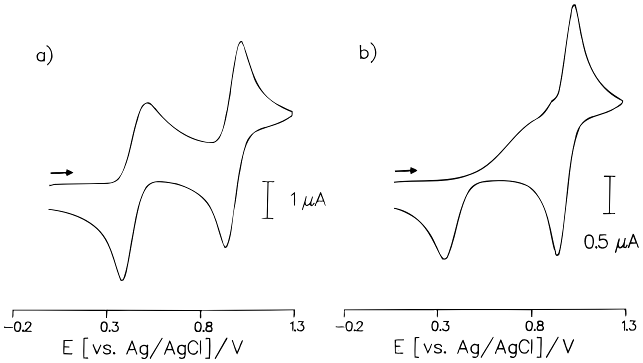

Figure 9. Cyclic voltammograms of **4** in liquid SO_2/0.1 M TBAPF$_6$, $c = 8 \times 10^{-4}$ M: (a) $T = -13$ °C, $v = 200$ mV s^{-1}; (b) $T = -50$ °C, $v = 100$ mV s^{-1}, freshly polished electrode.

freshly annealed platinum wire as the working electrode. Two oxidation peaks are visible at $E^1_{pa} = 0.700$ V and $E^2_{pa} = 0.950$ V with two corresponding reduction waves at $E^1_{pc} = 0.555$ V and $E^2_{pc} = 0.890$ V. At a scan rate of 20 mV s^{-1} the difference between E^1_{pa} and E^1_{pc} drops to 125 mV.

(d) 5,6 Dihydro-5,6-dimethylbenzo[*c*]cinnoline (4). Compound **4** dissolves in SO_2 ($c = 8 \times 10^{-4}$ M) with a yellow color, while the CH_2Cl_2 solution is colorless.

The cyclic voltammogram of **4** in SO_2 at −13 °C in the potential range between −0.06 V and 1.24 V shows two oxidation peaks at $E^1_{pa} = 0.470$ V and $E^2_{pa} = 0.965$ V and in the reverse sweep two corresponding reduction peaks at $E^1_{pc} = 0.350$ V and $E^2_{pc} = 0.900$ V (Figure 9a). While the second oxidation wave and the corresponding reduction wave have the normal shape of a cyclic voltammogram and the standard potential of the corresponding redox pair could be easily determined to be $E^0_2 = 0.940$ V, the broad shape of the first oxidation wave and the high ΔE_{p1} value of 120 mV are very unusual and allow a determination of E^0_1 only with the help of digital simulations.

Decreasing the temperature drastically changes the cyclic voltammograms. At −50 °C the first oxidation peak has shifted to 0.770 V, while the reduction peak at E^1_{pc} has moved to 0.270 V (Figure 9b). Furthermore, an additional shoulder on the cathodic side of the second oxidation wave appears at 0.850 V. The shapes of the second oxidation and the corresponding reduction wave are almost unchanged, but their position on the potential axis has shifted in the cathodic direction, so that E^0_2 now has a value of 0.905 V. A further decrease in temperature to −70 °C leads to the complete disappearance of the first oxidation peak below the second oxidation wave. The first

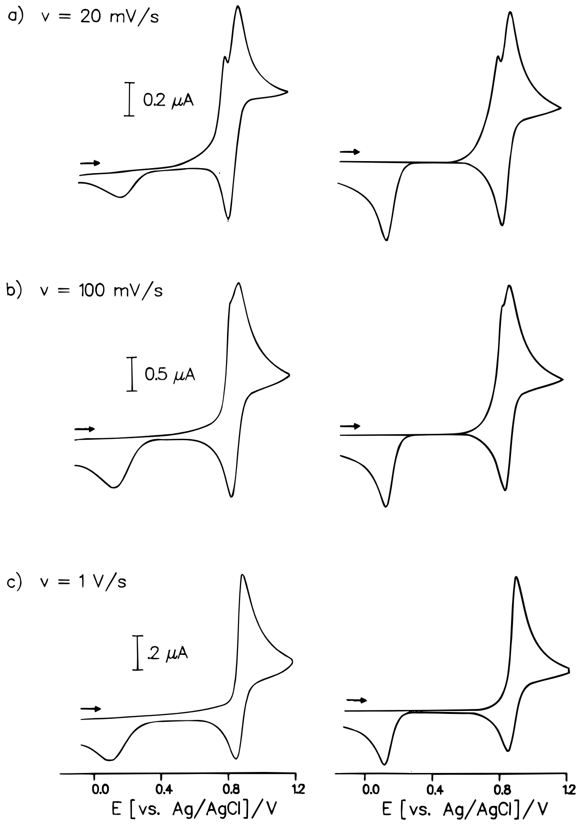

Figure 10. Experimental (left) and simulated (right) cyclic voltammograms for the oxidation of **4** in liquid SO_2/0.1 M $TBAPF_6$, $c = 8 \times 10^{-4}$ M, $T = -70$ °C: (a) $v = 20$ mV s^{-1}; (b) $v = 100$ mV s^{-1}; (c) $v = 1$ V s^{-1}; specific simulation data in supporting information (Table 12).

reduction wave shows a further shift in the cathodic direction (Figure 10).

The cyclic voltammograms of **4** in SO_2 at -70 °C and different scan rates are presented in Figure 10. At a sweep rate of 20 mV s^{-1} a spike at 0.830 V is visible (Figure 10a), which shifts in the anodic direction if the scan rate is increased. The spike changes to a shoulder on the rising part of the second oxidation wave (Figure 10b) in the range of 100 mV s^{-1} and finally disappears beneath this oxidation wave at 1 V s^{-1} (Figure 10c).

At -50 °C we succeeded in generating the trication of **4** at a standard potential of $E^0_3 = 3.270$ V during the cyclic voltammetric experiments in SO_2.

The voltammograms in CH_2Cl_2 at -60 °C show two reversible oxidation waves with the following standard potentials $E^0_1 = 0.295$ V and $E^0_2 = 0.875$ V.

The temperature- and scan-rate-dependent changes in the shapes of the voltammograms in CH_2Cl_2 are not as drastic as in SO_2.

During all measurements the shapes of the voltammograms turned out to be very sensitive to the condition of the platinum working electrode. The strongest shifts in potential of the first oxidation and the first reduction peaks could be observed at a freshly polished electrode. At a used electrode the first electron transfer seemed to be much more reversible. This contradicts "normal" experimental experience. Reproducible results could be obtained only at freshly polished electrodes.

3.3. Discussion of Different Electrochemical Reaction Mechanisms. Crystal structure and ESR/ENDOR investigations show that electron transfer reactions with these cyclic hydrazines are accompanied by structural changes of the molecular framework.

Scheme 1. ECE−EEC Mechanism; $|E^0_{A1}| > (|E^0_{B1} < |E^0_{B2}|)$

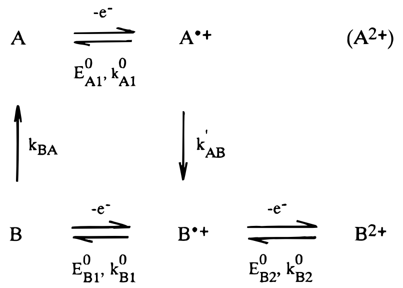

As mentioned in the Introduction, different electrochemical reaction mechanisms were discussed for the case of electron transfer reactions accompanied by structural changes. Any of these mechanisms might have explained the unusual shapes of the cyclic voltammograms of **3** and **4**. The following will describe our way of finding the correct reaction mechanism with the help of digital simulation as well as thermodynamic and kinetic considerations.

The first mechanism we will discuss here is the ECE−EEC−DISP mechanism (Scheme 1) which we proposed in our preliminary communication.[19] According to this reaction scheme, the neutral molecule A (a′a′ conformation regarding to the *N*,*N*′-phenyl or the *N*,*N*′-methyl substituents in the case of **3** or **4**) will be oxidized in a single electron transfer step to the radical cation $A^{\bullet+}$ of the same geometry at the redox potential E^0_{A1}. After this electron transfer, the molecular framework flattens to form the radical cation $B^{\bullet+}$. The conjugation between the N atoms in the flattened molecule is increased to such an extent that the standard potential E^0_{B2} of the redox pair $B^{\bullet+}/B^{2+}$ has a lower value than E^0_{A1}. Thus the cyclic voltammogram in Figure 5a shows only a single oxidation wave, which corresponds to the oxidation of A to $A^{\bullet+}$, the transformation of $A^{\bullet+}$ to $B^{\bullet+}$, and the further oxidation of $B^{\bullet+}$ to B^{2+}. In the reverse sweep the reduction of B^{2+} to neutral B, which transforms to the thermodynamically more stable A form in a following irreversible "chemical" reaction step, is visible (EEC sequence). The trace crossing, which appears in the cyclic voltammogram of Figure 5a can be explained with a fast homogeneous disproportionation reaction of the type

$$B^{2+} + A \underset{k_{-d}}{\overset{k_d}{\rightleftharpoons}} B^{\bullet+} + A^{\bullet+} \qquad (1)$$

Thermodynamically, the left side of this equilibrium is favored, but the homogeneous reaction, which transforms $A^{\bullet+}$ to $B^{\bullet+}$, controls the equilibrium kinetically. This kinetic control leads to an extraproduction of $B^{\bullet+}$ when the potential in the cyclic voltammetric experiment reaches the standard potential of the $B^{\bullet+}/B^{2+}$ redox pair. The additional anodic current, which occurs during the reverse sweep in the crossover region, is a result of the reoxidation of the extraproduced $B^{\bullet+}$.

The simulated cyclic voltammograms using this mechanism fit very well with the experimental voltammograms of **3**.[19]

Another promising mechanism is the E_iE−DISP mechanism (Scheme 2). According to this reaction scheme, the oxidation of the neutral compound A takes place with a small heterogeneous rate constant because of the conformational change of the molecule that occurs simultaneously with the charge transfer. The charge transfer step $A \rightarrow B^{\bullet+} + e^-$ does not have a measurable rate until the standard potential $E^0_{B^{\bullet+}/B^{2+}}$ is reached. Therefore, the cyclic voltammogram in Figure 5a shows only a single anodic wave, while in the reverse sweep, two cathodic waves, corresponding to the reduction of B^{2+} to $B^{\bullet+}$ and $B^{\bullet+}$

Scheme 2. $E_iE{-}DISP$ Mechanism; $|E_2^0| > |E_1^0|$, $k_1^0 \ll k_2^0$.

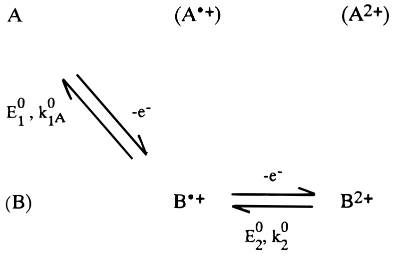

to A, are visible. Important for this mechanism is the disproportionation reaction

$$A + B^{2+} \underset{k_{-d}}{\overset{k_d}{\rightleftharpoons}} 2B^{\bullet+} \qquad (2)$$

The equilibrium constant of this reaction can be calculated on the basis of the thermodynamic standard potentials of the two electron transfer steps with the help of the following formula:[32,33]

$$K_{dis} = \exp\left[\frac{nF}{RT}(E^0_{B^{\bullet+}/B^{2+}} - E^0_{A/B^{\bullet+}})\right] \qquad (3)$$

If the difference between the standard potentials is positive, the equilibrium of the disproportionation reaction is on the side of the radical cations. As soon as the first dications are produced, they react with neutral molecules by generating radical cations. That means that a single radical cation, which will be heterogeneously oxidized, generates two radical cations via the comproportionation (disproportionation) reaction. Because of this homogeneous autocatalysis, the current during the forward sweep of the cyclic voltammograms increases strongly within a small potential range and reaches a much higher value than in the case of pure heterogeneous control. The heterogeneous control does not start until all of the neutral molecules within the diffusion layer have been consumed by the comproportionation reaction. The signal of this autocatalysis in a cyclic voltammogram is a spike.

We did not observe this spike effect during our cyclic voltammetric investigations of **3**. The voltammograms of **4** show such a spike only at low temperatures and low sweep rates (Figure 10). But this is not sufficient to exclude the $E_iE{-}$DISP mechanism from our considerations.

So far, we have assumed that homogeneous electron exchange reactions like the above-mentioned disproportionations have very high rate constants. Typical values for the rate constants of electron exchange reactions in the gas phase are in the range of 10^{12} and 10^{13} L mol^{-1} s^{-1}. Exceptions are electron exchange reactions between alkylhydrazines, whose rate constants are 3−4 orders of magnitude lower. Nelsen et al.[34] were able to determine the rate constant of the electron transfer reaction between the radical cation of the anti form and the neutral syn form of 8,8′-bis(8-azabicyclo[3.2.1]octane) in acetonitrile with the help of cyclic voltammetry. This constant had the surprisingly low value of 2.6×10^2 L mol^{-1} s^{-1}. Nelsen et al. confirm the low rate constants of the electron transfer reactions between alkylhydrazines in the gas phase as well as in solution with structural changes of the respective molecular frameworks, which take place simultaneously with the charge transfer reactions.

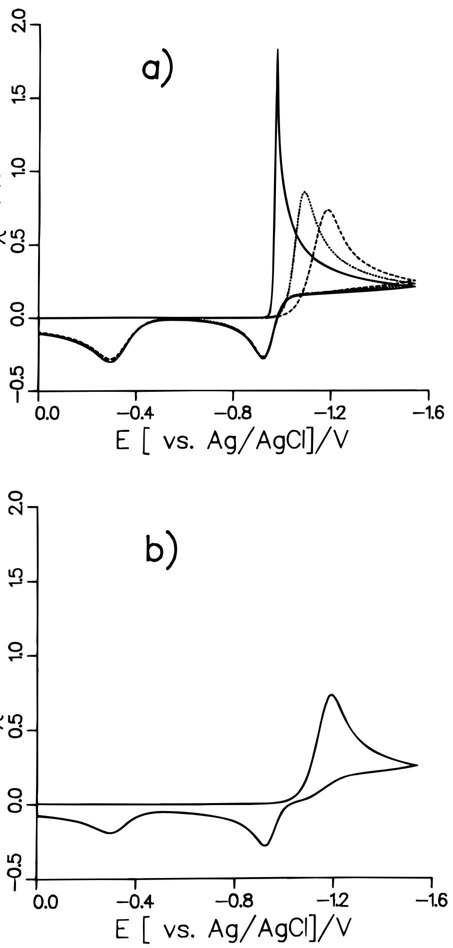

Figure 11. Digital simulation of an $E_iE{-}DISP$ mechanism. Simulation data: $E_1^0 = 0.830$ V, $\alpha_1 = 0.545$, $k_1^0 = 1.0 \times 10^{-7}$ cm s^{-1}; $E_2^0 = 1.000$ V, $\alpha_2 = 0.50$, $k_2^0 = 1.5 \times 10^{-2}$ cm s^{-1}, $D = 1.0 \times 10^{-5}$ cm^2 s^{-1}; $k_{-d} = k_d \times (6912)^{-1}$. (a) $k_d = 1600$ c^{-1} (—), 16 c^{-1} (- - -), 1.6 c^{-1} (•••) s^{-1}; (b) $k_d = 0$.

Figure 11 shows digital simulations of cyclic voltammograms on the basis of an $E_iE_d{-}$DISP mechanism with different rate constants k_d of the disproportionation reaction at constant K_{dis}. It is obvious that the oxidation wave loses its spike character with decreasing k_d and shifts toward anodic potentials. At rate constants in the range 16/c s^{-1} (c = concentration of the substrate), the shape of the oxidation wave is the same as in the case of a purely heterogeneously controlled charge transfer reaction. Moreover, the simulations reveal that under certain conditions the disproportionation reaction leads to a trace crossing effect without the simultaneous appearance of the spike effect.

Thus, the E_iE mechanism with a slow disproportionation reaction is a promising candidate to explain the shapes of the cyclic voltammograms of **3** and **4**, and we actually succeeded in simulating the experimental voltammograms of **3** and **4** on the basis of this mechanism with reasonable kinetic and thermodynamic parameters. Figures 6−10 (Figures 1−4 in the supporting information) show both the experimental and the computer-simulated voltammograms.

In comparing the two mechanisms, some serious experimental and theoretical reasons speak in favor of the $E_iE{-}$DISP mechanism.

Firstly, in the case of both mechanisms, the changes of the multisweep voltammograms of **3** (Figure 8) as temperatures rise

---

[32] Heinze, J. *Angew. Chem., Int. Ed. Engl.* **1984**, *23*, 831−847; *Angew. Chem.* **1984**, *96*, 823−840.

[33] Laviron, E. *J. Electroanal. Chem.* **1983**, *148*, 1−16.

[34] Nelsen, S. F.; Cunkle, G. T.; Evans, D. H.; Haller, K. J.; Kaftory, M.; Kirste, B.; Kurreck, H.; Clark, T. *J. Am. Chem. Soc.* **1985**, *107*, 3829−3839.

Scheme 3. Square Redox Scheme Assuming Homogeneous Equilibria for the Neutral and the Cationic Species

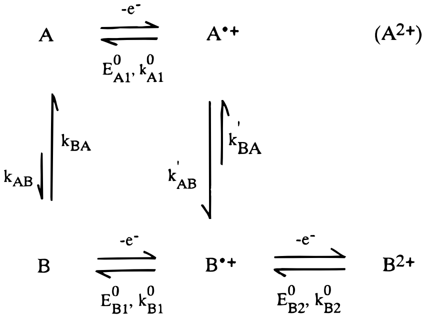

are explained by an increase in the rates of the corresponding disproportionation reactions. But even at very high disproportionation rates, digital simulations of the ECE−EEC−DISP mechanism in agreement with thermodynamic and kinetic considerations never showed such a rapid decrease in the intensity of the oxidation wave at E^1_{pa} as observed in the case of compound **3** at −30 °C. On the other hand, there is very close agreement between the simulations of the multisweep voltammograms on the basis of the E_iE−DISP mechanism and the experimental voltammograms (Figure 8). These results are sufficient to exclude the ECE reaction scheme.

Secondly, the cyclic voltammetric experiments with a platinum wire as the working electrode also contradict the ECE−EEC−DISP mechanism (Figure 7b). The attempt to explain these voltammograms with the help of the ECE−EEC−DISP mechanism leads to the conclusion that the oxidation peak at E^1_{pa} and the reduction wave at E^1_{pc} belong to different conformations and therefore to different electron transfer steps, which are followed by fast conformational changes in the molecular framework. The reaction steps $A \rightarrow A^{\bullet+} + e^- \rightarrow B^{\bullet+}$ and $B^{\bullet+} + e^- \rightarrow B \rightarrow A$ can be described as E_rC_i reactions. In the kinetically controlled region of such a reaction, the equation for the peak potential is as follows:[35]

$$E_p = E_{1/2} - \frac{RT}{nF}0.780 + \frac{RT}{2nF}\ln\left[\frac{RT}{nF}\frac{k}{v}\right] \qquad (4)$$

The scan rate dependence of the potential difference $E^1_{pa} - E^1_{pc}$ derived from this equation is much higher than the observed one.

Thus, *fast* conformational changes following the electron transfer reactions can be ruled out. But there are also some arguments against *slow* follow-up reactions. The ECE−EEC−DISP mechanism with slow chemical reactions is only possible if the two conformations have nearly identical standard potentials for the formation of the corresponding radical cations. The irreversibility of the homogeneous follow-up reactions surely requires high ΔG values and, therefore, high standard potential differences. Moreover, in the case of a slow reaction $B \rightarrow A$, the multisweep voltammograms of **3** in SO_2 at the platinum disc electrode should show an additional oxidation peak corresponding to the oxidation of B. But this was never observed in the voltammograms of **3**.

The same arguments hold for compound **4**. Therefore, it was not possible to simulate and explain the voltammograms of **3** and **4** on the basis of an ECE−EEC−DISP mechanism involving the irreversible steps $A^{\bullet+} \rightarrow B^{\bullet+}$ and $B \rightarrow A$ with thermodynamically and kinetically meaningful parameters.

The introduction of a square reaction scheme with reversible chemical steps (Scheme 3) offers a new strategy for the mechanistic interpretation of the experimental data.

X-ray structure analyses reveal for **2** an a′e′ and for **3** an a′a′ conformation in the solid state. ^{1}H-NMR investigations of the dihydrocinnolines do not allow a clear decision on whether there is also only one conformation present in solution or whether there is a fast equilibrium between different conformations. On the assumption that in case of **3** and **4** the main component in solution is the a′a′ conformation A, which is in fast equilibrium with a cation-like a′e′ or e′e′ conformation B, the explanation of the cyclic voltammograms of **3** and **4** is shown in reaction scheme 3.

Because of its cation-like structure, the conformation B has a lower oxidation potential than A. If the potential during a cyclic voltammetric experiment reaches the standard potential E^0_{B1}, B will be oxidized to $B^{\bullet+}$, and will therefore be withdrawn from the equilibrium between A and B. At "high" temperatures, which in the case of **4** means at temperatures above −70 °C, the rate constant k_{AB} has such a high value that B is steadily generated by the equilibrium reaction. Thus the oxidation wave at E^1_{pa} in Figures 9 and 10 should represent the oxidation of a species which is thermodynamically less favored and in solution is only present in small amounts.

At low temperatures, the rate at which B is produced by the equilibrium reaction is not fast enough. Thus the cyclic voltammograms show only one oxidation wave, which should represent the following ECE sequence:

$$A \xrightarrow{-e^-} A^{\bullet+} \rightarrow B^{\bullet+} \xrightarrow{-e^-} B^{2+} \qquad (5)$$

This is valid only if the oxidation of A occurs at a measurable rate once the standard potential E^0_{B1} has been reached.

But the experimental observations contradict this mechanism. With decreasing temperature or increasing scan rate, the oxidation peak at E^1_{pa} should become less intense, while at the same time a new oxidation wave, corresponding to the production of $A^{\bullet+}$, should occur. Assuming that this new oxidation wave is positioned below the oxidation peak of the B^{2+} formation, with decreasing temperature, this wave should increase in intensity relative to E^1_{pa}. But this was never observed. With decreasing temperature the oxidation peak at E^1_{pa} shows only a shift in anodic direction. In accordance with these results Nelsen et al.[36] stated from theoretical AM1 calculations that a twisted $A^{\bullet+}$ has no energy minimum and therefore a square scheme would not be very conceivable.

Another possibility is that a CE_iE−DISP mechanism [equilibrium between the a′a′ and the a′e′(e′e′) conformations of the neutral species **3** or **4**] is valid over the whole temperature range investigated. This reaction type which corresponds to a triangular scheme has been discussed by Nelsen and Evans[36] for the structurally related hexahydropyridazine derivatives. Although cyclic voltammetric experiments and simulations cannot rule out the existence of a fast equilibrium between different conformations of the dihydrocinnolines in solution, both thermodynamic and kinetic considerations, as well as the absence of any proof of the existence of B, are strong evidence for the "simple" E_iE−DISP mechanism which substitutes the ECE−EEC−DISP mechanism which substitutes the ECE−EEC−DISP mechanism proposed formerly[19] on the basis of inadequate experimental data.

3.4. Results of the Digital Simulations on the Basis of the E_iE−DISP Mechanism. Table 4 shows the values of the homogeneous and heterogeneous electron transfer steps connected with the formation of the mono- and dications of **3** in CH_2Cl_2, which were determined with the help of digital

---

(35) Ryan, M. D.; Wilson, G. S. *Anal. Chem.* **1982**, *54*, 20R−27R.

(36) Nelsen, S. F.; Chen, L.-J.; Petillo, P. A.; Evans, D. H.; Neugebauer, F. A. *J. Am. Chem. Soc.* **1993**, *115*, 10611−10620.

Table 4. Diffusion Coefficients and Data of the Heterogeneous and Homogeneous Electron Transfer Reactions of **3** in CH_2Cl_2/0.1 M TBAPF$_6$ at Various Temperatures[a]

T (°C)	$E_2^0 - E_1^0$ (V)	D (cm^2 s^{-1})	α_1	k_1^0 (cm s^{-1})	α_2	k_2^0 (cm s^{-1})	K_{dis}	k_d (L M^{-1} s^{-1})	k_{-d} (L M^{-1} s^{-1})
+20	0.310	4.6×10^{-6}	0.33	1.3×10^{-4}	0.50	6.5×10^{-2}	2.1×10^{5}	1.4×10^{5}	6.7×10^{-1}
+20[b]	0.310	4.6×10^{-6}	0.33	1.6×10^{-3}	0.50	6.5×10^{-2}			
−30	0.285	2.3×10^{-6}	0.42	8.3×10^{-7}	0.50	7.6×10^{-3}	8.1×10^{5}	1.8×10^{3}	2.2×10^{-3}
−50	0.275	1.4×10^{-6}	0.41	1.3×10^{-7}	0.50	4.2×10^{-3}	1.6×10^{6}	1.8×10^{2}	1.1×10^{-4}
−80	0.260	3.6×10^{-7}	0.43	8.4×10^{-10}	0.50	4.8×10^{-4}	6.1×10^{6}	9	1.5×10^{-6}

[a] All kinetic data were determined by digital simulation and subsequent fitting procedures, assuming an E$_i$E−DISP mechanism. Normally, the experimental voltammograms were obtained by measurements at "old" Pt electrodes. [b] Freshly annealed Pt wire electrode.

simulations on the basis of the E$_i$E−DISP mechanism. Similar values are obtained for the electrochemical oxidation of **3** in SO_2.

As can be seen, the heterogeneous rate constants k_1^0 of the monocation formation are some orders of magnitude smaller than the corresponding values k_2^0 of the dication formation within the temperature range of the experiments. This is generally valid for all investigated compounds.

The activation energies determined from Arrhenius plots are 13.4 ± 0.5 kcal mol^{-1} for the first and 5.4 ± 0.3 kcal mol^{-1} for the second heterogeneous electron transfer and 10.9 ± 0.8 kcal mol^{-1} for the disproportionation reaction. This confirms the theory that the heterogeneous and homogeneous formation of the monocation is impeded by a simultaneously occurring structural reorganization of the molecular framework.

Digital simulations using the data of Table 4 match the experimental voltammograms of **3** in CH_2Cl_2 at different temperatures very well, as can be seen in Figure 6. The multisweep voltammograms of **3** in CH_2Cl_2 at −30 and −80 °C (Figure 8) could be simulated with the same data.

The occurrence of a current shoulder on the rising part of the oxidation peak in the voltammograms of **3** in CH_2Cl_2 as the substrate concentration increased, which was explained by an increase in the disproportionation rate, can also be simulated without any change in the simulation parameters, except for the concentrations (Figure 7a and supporting information).

To obtain a good fit with the voltammogram of **3** in CH_2Cl_2 at the platinum wire electrode (Figure 7b and supporting information) using the simulation parameters of the corresponding voltammograms obtained at the platinum disk electrode (Figure 6, Table 4), only the heterogeneous rate constant k_1^0 had to be changed from 1.3×10^{-4} to 1.6×10 cm s^{-1}. The fact that no change in k_2^0 was necessary for a good fit leads to the conclusion that electron transfer reactions at an annealed platinum wire are not, in general, faster than reactions at a polished platinum disk. A possible explanation of this behavior is that the annealing of the platinum wire produces a thin layer of oxide. This layer catalyzes the conformational change of **3** at the surface of the electrode and therefore increases the rate of the first electron transfer. The second electron transfer reaction as well as the homogeneous charge transfer reactions are not affected by this catalysis.

Simulated voltammograms of compound **4** fit all the experimental data very well. Even the spike effect which is typical for the autocatalytic generation of the radical cation B$^{\bullet+}$ could be simulated with great accuracy. Further details of the simulations are placed in the supporting information.

In the case of all investigated compounds, the heterogeneous rate constants of the first electron transfer step are much smaller and the corresponding activation energies much higher than the respective values of the dication formation (Table 4). Details of the rate constants and activation parameters are presented in the supporting information.

Table 5. Extrapolated Redox Potentials of the Compounds **1**−**10** in SO_2 and CH_2Cl_2 at 25 °C

compd	solvent	E_1^0 (V)	E_2^0 (V)	E_3^0 (V)
1	SO_2	0.795	1.690	
2	SO_2	0.560	1.240	2.820
	CH_2Cl_2	0.485	1.220	
3	SO_2	0.755	1.000	
	CH_2Cl_2	0.610	0.920	
4	SO_2	0.395	0.975	3.345
	CH_2Cl_2	0.295	0.900	
5	SO_2	0.465	0.930	
6	SO_2	0.150	0.805	3.325
	CH_2Cl_2	−0.070	0.740	
7	SO_2	0.120	0.695	3.040
	CH_2Cl_2	−0.135	0.635	
8	CH_2Cl_2	−0.150	0.590	
9	SO_2	0.330	0.795	2.955
10	CH_2Cl_2	−0.135	0.505	

Nelsen and Evans[2] found a correlation between the torsional angle θ of the N lone pairs and the k_1^0 values of different aliphatic hydrazines. The k_1^0 values are smaller when the torsion angle θ between the orbital axes of the lone pairs on the nitrogens in the neutral state of the molecules differs from the structure of the radical cation. The same behavior is not easy to detect in the case of the dihydrocinnolines because these compounds have not only different torsional angles but also different conformational mobilities owing to the varied bridging. So, it is obvious that compound **3** with a torsional angle θ of 89° has much smaller k_1^0 values under the same environmental conditions than compound **7**, whose structure in the neutral state (see the crystal structure of **10**, $\theta = 175°$) clearly resembles the radical cation conformation ($\theta = 0°$ or 180°). But compound **2** with a torsional angle θ of 60° and with a very high rate constant k_1^0 relative to **3** and **7** does not fit into this scheme. This can be explained by the low internal reorganization energy required for the completely bridged framework. Further studies are in progress.

3.5. Discussion of the Potentials. To be able to compare the oxidation potentials of the investigated dihydrocinnolines, the standard potentials at 25 °C were calculated with the data of the ferrocene calibrations on the assumption of a temperature-dependent potential shift of the standard potential E_2^0 of the second electron transfer step of 1 mV °C^{-1} in SO_2 and 0.5 mV °C^{-1} in CH_2Cl_2 (Table 5).

In the case of all dihydrocinnolines, the values of the standard potentials in SO_2 are always higher than the respective values in CH_2Cl_2. A possible explanation for this phenomenon is the ability of SO_2 to form charge-transfer complexes with aromatic and nitrogen compounds.[37−39] The yellow or orange colors of the solutions of the dihydrocinnolines in SO_2 are a clear indication of the formation of complexes. This complexation further stabilizes the neutral states of the molecules, and this leads to higher oxidation potentials in SO_2 in comparison to CH_2Cl_2.

---

(37) Booth, D.; Dainton, F. S.; Ivin, K. J. *Trans. Faraday Soc.* **1959**, *55*, 1293−1309.

(38) Hata, T.; Kinumaki, S. *Nature* **1964**, *203*, 1378−1379.

(39) Purrington, S. T.; Wilder, P. *J. Org. Chem.* **1965**, *30*, 2070−2072.

Owing to the nearly planar biphenyl-2,2′-diyl bridges in **2**, a smaller internal reorganization energy than in the case of compound **1** or **3** is required for the electron transfer. Furthermore, the N lone pairs in **2** ($\theta = 60°$) interact more strongly with each other than the respective orbitals in **1** (free mobility; in the crystal $\theta = 74°$) and **3** ($\theta = 89°$). Therefore the first electron transfer of **2** may be accompanied by release of lone-pair repulsion.

The relatively lower first oxidation potentials of the 5,6-dihydro-5,6-dimethylbenzo[*c*]cinnoline (**4**) and the 2,3-dihydro-1*H*-benzo[*c*]pyrazolo[1,2-*a*]cinnolines **6**, **7**, **8**, and **10** are the result of the nearly planar molecular framework which undergoes only little changes in the first electron transfer. Correspondingly, larger potentials E_1^0 are observed, when the planar arrangement is affected by specific, space demanding substitution, e.g. by the 1,10-methyl groups in **5** or the 8,9-methyl groups in **9**.

The 2,3-dihydro-1*H*-benzo[*c*]pyrazolo[1,2-*a*]cinnolines show the following sequence of standard potentials for the first and second electron transfer:

$$E_1^0\text{: } \mathbf{8} < \mathbf{7} = \mathbf{10} < \mathbf{6} < \mathbf{9}$$

$$E_2^0\text{: } \mathbf{10} < \mathbf{8} < \mathbf{7} < \mathbf{6} = \mathbf{9}$$

The sequence of the standard potentials of the radical cation formation can be explained by a strong localization of the positive charges on the N atoms of the dihydrocinnolines. The most pronounced cation stabilizing effect of methyl groups will be expected in para position relative to the electron-deficient center. Therefore, the radical cation of the 7,10-dimethyl-substituted compound **8** is the best stabilized one with the lowest standard potential E_1^0. The high standard potential of compound **9** with methyl groups in 8- and 9-positions indicates that, in this case, the cation-stabilizing effect of the methyl groups is suspended by steric effects.

The strongest influence of the substituents is measured in the case of the trication formation because in this case the charge is removed not from the lone pairs on the N atoms but from the 5,6-dihydrobenzo[*c*]cinnoline framework. Therefore, the standard potential E_3^0 of compound **7** is 285 mV lower than the corresponding standard potential of the primary compound **6**.

In agreement with the results of Nelsen and Evans[2] obtained from studies of aliphatic hydrazines and their later interpretation,[40] we find in the investigated dihydrocinnoline series the following correlation between the standard potentials of the first electron transfer reactions and the torsional angle θ of the neutral state of these molecules. The more the torsional angle of the neutral species resembles the torsional angle of the radical cation ($\theta = 0°$, 180°), the lower is the observed standard potential E_1^0. The explanation for this is that a radical-cation-like structure of the neutral molecule leads to the strongest possible destabilizing interaction between the lone pairs on the N atoms and requires only little internal reorganization on oxidation. Therefore, compound **3**, with the strongest deviation from the radical cation structure, shows the highest oxidation potential E_1^0, while the 2,3-dihydro-1*H*-benzo[*c*]pyrazolo[1,2-*a*]cinnolines (**6**−**10**) with their radical-cation-like structures are oxidized at lower potentials. The standard potential E_1^0 of compound **2**, which has a torsional angle θ of 60°, lies between the above cases.

4. Conclusions

The unusual shape of the voltammograms of the investigated 5,6-dihydro[*c*]cinnolines can be explained by an E_iE−DISP mechanism with a slow disproportionation reaction. Combining cyclic voltammetric experiments and digital simulations enabled us not only to elucidate the best fitting reaction mechanism but also to perform a quantitative analysis of the heterogeneous and homogeneous electron transfer steps.

Acknowledgment. This work was supported by the Deutsche Forschungsgemeinschaft, the Volkswagenstiftung, and the Fonds der Chemischen Industrie.

Supporting Information Available: Tables of positional parameters and anisotropic thermal parameters and listings of structure factors for **3** and **10**, NMR data for **2**−**6** and **9**, and tables and figures of electrochemical results (25 pages). This material is contained in many libraries on microfiche, immediately follows this article in the microfilm version of the journal, can be ordered from the ACS, and can be downloaded from the Internet; see any current masthead page for ordering information and Internet access instructions.

JA952722+

---

[40] Nelsen, S. F. *Acc. Chem. Res.* **1981**, *14*, 131−138.